

# Study of Excited $\Xi$ Baryons in $\bar{p}p$ -Collisions with $\overline{\text{PANDA}}$

Authors:

Jennifer Pütz, Albrecht Gillitzer, James Ritman

# Abstract

Understanding the excitation pattern of baryons is indispensable for a deep insight into the mechanism of non-perturbative QCD. Up to now only the nucleon excitation spectrum has been subject to systematic experimental studies while very little is known on excited states of double or triple strange baryons.

In studies of antiproton-proton collisions the  $\overline{\text{PANDA}}$  experiment is well-suited for a comprehensive baryon spectroscopy program in the multi-strange and charm sector. A large fraction of the inelastic  $\bar{p}p$  cross section is associated to final states with a baryon-antibaryon pair together with additional mesons, giving access to excited states both in the baryon and the antibaryon sector.

In the present study we focus on excited  $\Xi$  states. For final states containing a  $\Xi \bar{\Xi}$  pair cross sections up to the order of  $\mu\text{b}$  are expected, corresponding to production rates of  $\sim 10^6/\text{d}$  at a Luminosity  $L = 10^{31} \text{ cm}^{-2} \text{ s}^{-1}$  (5% of the full value). A strategy to study the excitation spectrum of  $\Xi$  baryons in antiproton-proton collisions will be discussed. The reconstruction of reactions of the type  $\bar{p}p \rightarrow \Xi^* \bar{\Xi}$  (and their charge conjugated) with the  $\overline{\text{PANDA}}$  detector will be presented based on a specific exemplary reaction and decay channel.

---

# Contents

<b>1</b>	<b>Event generation</b>	<b>1</b>
<b>2</b>	<b>Analysis</b>	<b>5</b>
2.1	Final state particle . . . . .	5
2.2	Reconstruction of $\Lambda^0$ and $\bar{\Lambda}^0$ . . . . .	5
2.3	Reconstruction of $\Xi$ and $\bar{\Xi}$ . . . . .	9
2.4	Reconstruction of $\Xi(1820)$ and $\bar{\Xi}(1820)$ . . . . .	15
2.5	Reconstruction of hole chain . . . . .	20
<b>3</b>	<b>Background</b>	<b>25</b>
<b>4</b>	<b>Conclusion</b>	<b>26</b>
	<b>Literature</b>	<b>27</b>

---

# 1 Event generation

To study excited  $\Xi$  baryons the simulation of signal events is needed. For this study 1.5 million signal events have been generated. The decay channel for the simulation is shown in figure 1.1.

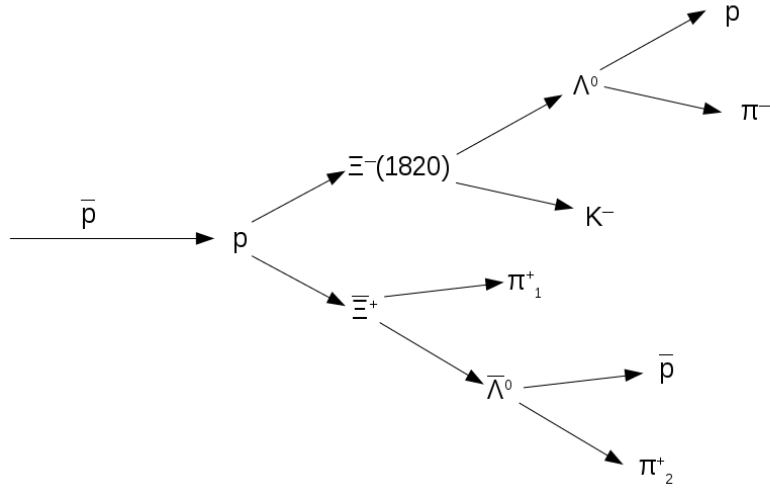


**Figure 1.1:** Simulated decay channel

For the charge conjugated channel further 1.5 million events were generated. The used parameters for the event generation are shown in table 1.1.

The chosen beam momentum of  $p_{\bar{p}} = 4.6 \text{ GeV}/c$  is 100 MeV above the production threshold of  $\Xi(1820)$  and  $\bar{\Xi}$ . The production cross section is expected to be of the same order ( $\sim \mu\text{b}$ ) as for  $\Xi$  [1].

**Table 1.1:** Parameter for event generation

Parameter	Value
Beam momentum	4.6 GeV/c <sup>2</sup>
Production	PHSP
Tracking	Ideal
Particle ID	Ideal

**Table 1.2:** Used software versions

Software	Version
FairSoft	mar15
FairRoot	v-15.03a
PandaRoot	trunk revision 28555
Geant	3
Genfit	1

The used software versions for Pandaroot and the external software package is listed in table 1.2

Since now  $\Xi(1820)$  was not defined in the evt.pdl file. The Lines in the code snippet 1.1 show how the particle is added to the file. The properties of  $\Xi(1820)$  coming from [2] are written down in table 1.3.

**Listing 1.1:** snippet from evt.pdl

```
add p Particle Xi(1820)- 23314 1.8230000e+00 2.4000000e-02
    2.0000000e-01 -3 3 0.0000000e+00 23314
add p Particle anti-Xi(1820)+ -23314 1.8230000e+00 2.4000000e-02
    2.0000000e-01 3 3 0.0000000e+00 -23314
```

**Table 1.3:** Properties of  $\Xi(1820)$  and  $\bar{\Xi}(1820)$ . The values are taken from [2]

Particle	J	I	P	Charge	Mass	Width
$\Xi(1820)$	$\frac{3}{2}$	$\frac{1}{2}$	(-1)	(-1)	$(1.823 \pm 5)\text{GeV}/c^2$	$(0.024 \pm 6)\text{ GeV}$
$\bar{\Xi}(1820)$	$\frac{3}{2}$	$\frac{1}{2}$	(-1)	1	$(1.823 \pm 5)\text{GeV}/c^2$	$(0.024 \pm 6)\text{ GeV}$

The generated transverse momentum against the longitudinal momentum for  $\Lambda^0$ ,  $\bar{\Lambda}^0$ ,  $\Xi$  and  $\Xi(1820)$  is presented in figure 1.2

Figure 1.4 shows the Dalitz plot for the  $\Lambda^0$ ,  $K^-$  and  $\bar{\Xi}$  final states for the channel  $\bar{p}p \rightarrow \Xi(1820) \bar{\Xi}$ .

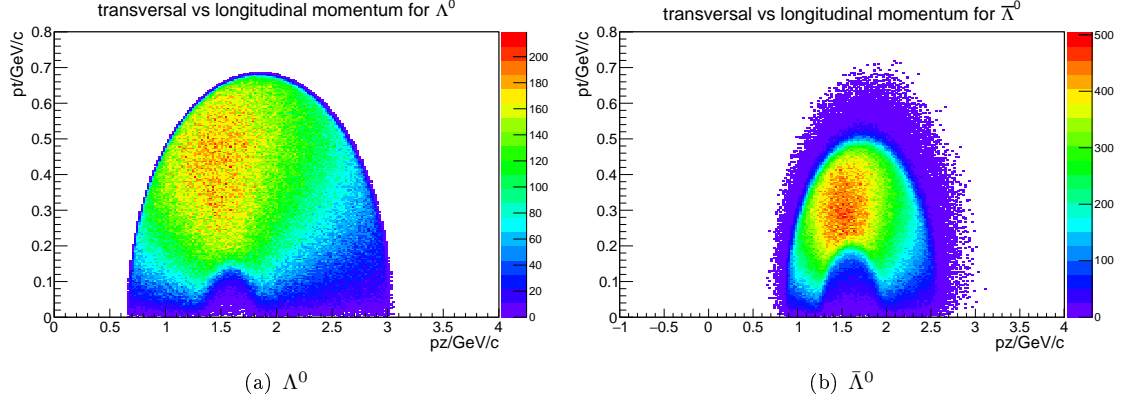


**Figure 1.2:** Figure a) shows the transverse momentum on the y axis against the longitudinal momentum on the x axis for  $\Lambda^0$ . Figure b) shows the same distribution for  $\bar{\Lambda}^0$ .

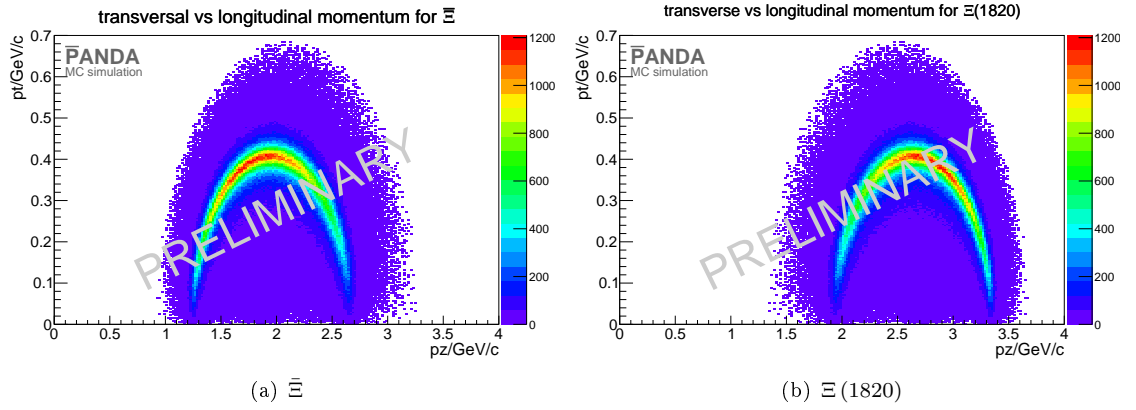


**Figure 1.3:** Figure a) shows transverse against the longitudinal momentum distribution for  $\Xi$ . Figure b) transverse versus longitudinal momentum distribution for  $\Xi(1820)$ .

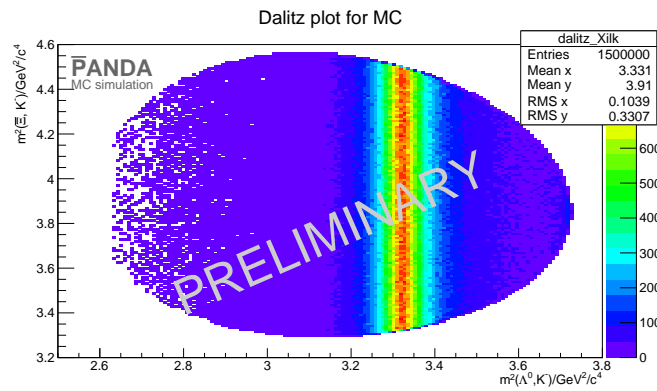


**Figure 1.4:** Dalitz plot for simulation. On x axis is the mass square of  $\Lambda^0$  and  $K^-$  and on the y axis there is the mass square of  $\Xi^-$  and  $K^-$

---

## 2 Analysis

To reconstruct all the simulated particles we start with the final state particles and go backwards through the reaction chain.

### 2.1 Final state particle

The selected final state particles are protons, antiproton,  $\pi^-$ ,  $\pi^+$ ,  $K^-$  and  $K^+$  mesons. For the reconstruction of these final state particles I used an ideal tracking. To make the selection a bit more realistic only particles with more than 3 hits in any inner tracking detector (MVD, STT and GEM) are selected. The selection criterion is chosen because three hits are defining a circle. A fourth hit point is then a validation of the track hypothesis.

The particle identification (PID) is also ideal. The selection criterion is set to 'best'.

The reconstruction efficiency for the final state particles is shown in table 2.1 and figure

2.1.

Table 2.2 shows the reconstruction efficiency for the c.c. channel.

### 2.2 Reconstruction of $\Lambda^0$ and $\bar{\Lambda}^0$

#### Selection

For the reconstruction of

- $\Lambda^0$  a proton and a  $\pi^-$  meson are combined and

**Table 2.1:** reco efficiency and momentum resolution for  $\bar{p}p \rightarrow \Xi(1820) \bar{\Xi}$

final state	N/%	$\frac{\sigma p}{p}/\%$
$\pi^-$	83.48	1.53
$\pi_1^+ (\bar{\Xi})$	80.93	1.38
$\pi_2^+ (\bar{\Lambda}^0)$	83.07	1.49
$K^-$	78.59	1.58
p	84.39	1.61
$\bar{p}$	78.25	1.61



**Table 2.2:** reco efficiency and momentum resolution for  $\bar{p}p \rightarrow \Xi(1820) \Xi$

final state	N/%	$\frac{\sigma_p}{p}/\%$
$\pi^+$	82.9625	1.54131
$\pi_1^- (\Xi)$	80.395	1.37697
$\pi_2^- (\Lambda^0)$	82.6867	1.48918
$K^+$	83.2709	1.57882
p	80.7079	1.55197
$\bar{p}$	80.9253	1.60091

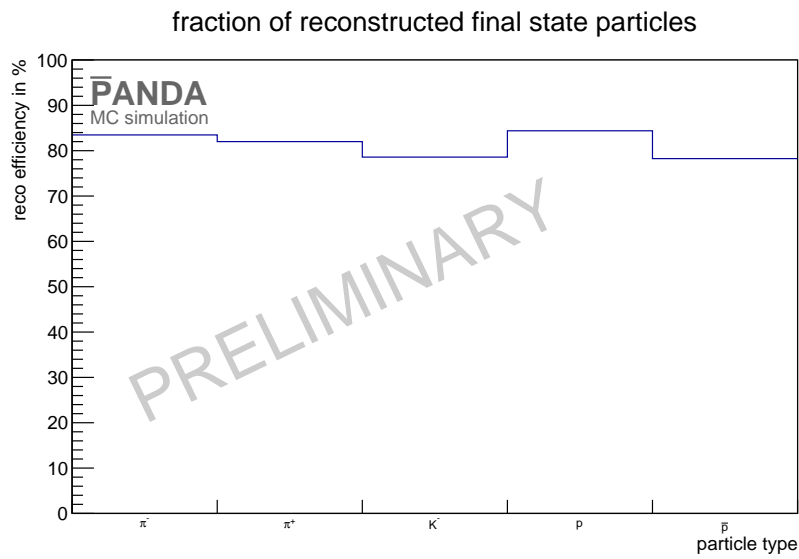


**Figure 2.1:** Reconstruction efficiency for final state particles. The x axis shows the particle type. On the y axis is shown the fraction of reconstructed particles, like it is shown in table 2.1

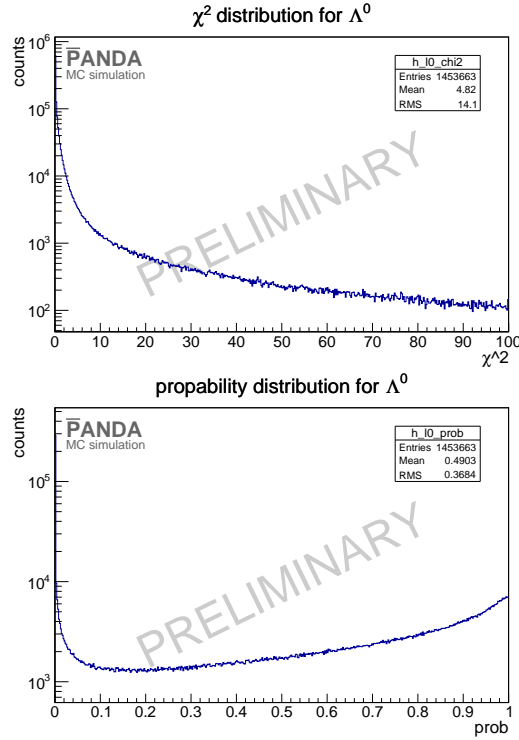


**Figure 2.2:** upper:  $\chi^2$  distribution; lower:  $\chi^2$  probability distribution

- for the reconstruction of  $\bar{\Lambda}^0$  a  $\bar{p}$  and a  $\pi^+$  are combined.

After the combination of the daughter particles a mass window cut is performed. Only those particles are chosen which have a mass within  $0.3\text{GeV}/c^2$ .

A vertex constraint fit with the PndKinVtxFitter is performed on the selected particle. This means that the tracks of the daughter particles are fitted to a common vertex point. The  $\chi^2$  and  $\chi^2$ -Probability distribution of the vertex fit for  $\Lambda^0$  is shown in figure 2.2.

In the  $\chi^2$ -probability distribution one can see a increasing number of events for probabilities going to one. These feature is not coming from vertex fitting. There is still a problem with covariance matrices which causes the effect.

The fit information coming from the vertex fit are used to perform a mass constraint fit with the kinematic fitter PndKinFitter. After using both fitter the selection criterion is set. One select only those particles which have a probability greater than 1% in both fitter. A scheme which shows how the events are selected can be found in figure 2.3.

If there is more than one candidate left after the cuts the best fitted candidate is chosen.

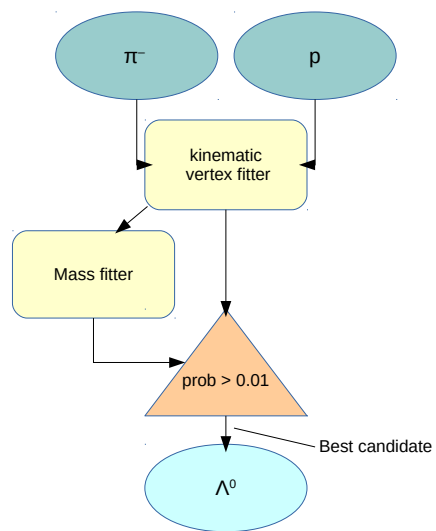


**Figure 2.3:** Scheme for  $\Lambda^0$  reconstruction

## Results

This subsection presents the results for the  $\Lambda^0$  and  $\bar{\Lambda}^0$  selection with the selection criteria introduced above. The mass distributions for different cuts are shown in figure 2.4 and figure 2.5.

The reconstructed mass can be derived by performing a double Gaussian fit on the cut mass. The mass distribution and the double Gaussian fit are exemplarily shown for  $\Lambda^0$  in figure 2.6

The mean value of the inner Gaussian fit is the reconstructed mass. The result for  $\Lambda^0$  is  $m_{\Lambda^0} = (1.116 \pm 3.5 \cdot 10^{-5}) \text{ GeV}/c^2$  and for  $\bar{\Lambda}^0$ :  $m_{\bar{\Lambda}^0} = (1.116 \pm 1 \cdot 10^{-5}) \text{ GeV}/c^2$ . The small fit errors could be a result from the wrong covariance matrices. But this has to be checked. Figure 2.7 shows the transverse momentum versus the longitudinal momentum.

After all cuts the reconstruction efficiency for  $\Lambda^0$  is 50.33% and for  $\bar{\Lambda}^0$  41.46%. The difference of the reconstruction efficiency of  $\Lambda^0$  and  $\bar{\Lambda}^0$  is caused by the difference between the decay length of their mother particles.  $\Lambda^0$  is emitted by the  $\Xi(1820)$  which has a very short decay length while the decay length of  $\Xi$  and  $\bar{\Xi}$  is  $c\tau = 4.91 \text{ cm}$  [2]. In addition the decay length of  $\Lambda^0$  and  $\bar{\Lambda}^0$  is  $c\tau = 7.98 \text{ cm}$ . If one sum this number up the final state particles of  $\bar{\Lambda}^0$  are produced more downstream than the final state particles of  $\Lambda^0$ . This can be also seen in figure 2.8. The finale state particles coming from  $\bar{\Lambda}^0$  are produced at the edge of the MVD detector so that the reconstruction efficiency get worse.

## 2.3 Reconstruction of $\Xi$ and $\bar{\Xi}$

### Selection

The reconstruction of  $\Xi$  and  $\bar{\Xi}$  fellow a similar scheme like for  $\Lambda^0$  and  $\bar{\Lambda}^0$ . For  $\bar{\Xi}$  are  $\bar{\Lambda}^0$  and  $\pi_1^+$  recombined and for  $\Xi$  in the c.c. channel  $\Lambda^0$  and  $\pi_1^-$ . Now it is distinguished between the to  $\pi^+$  ( $\pi^-$ ) particle and use only those particles which have not already been combined. After combining the daughter particles it is performed a mass window cut with width of  $0.3 \text{ GeV}/c^2$  around the  $\Xi$  mass  $m_{\Xi} = 1.32171 \text{ GeV}/c^2$  [2].

The fitting scheme is the same as for  $\Lambda^0$  and  $\bar{\Lambda}^0$  and is shown in figure 2.9 After the mass window cut the daughter particles are fitted to a common vertex with the PndKinVtxFitter. And again these information is used to perform the mass constraint fitter.

Only those particles are selected which have a  $\chi^2$  probability of more than 1 % in both fitter. Figure 2.10 shows exemplarily the cut on the vertex fit probability.

If there is more than one candidate left after all cuts the best candidate is chosen.

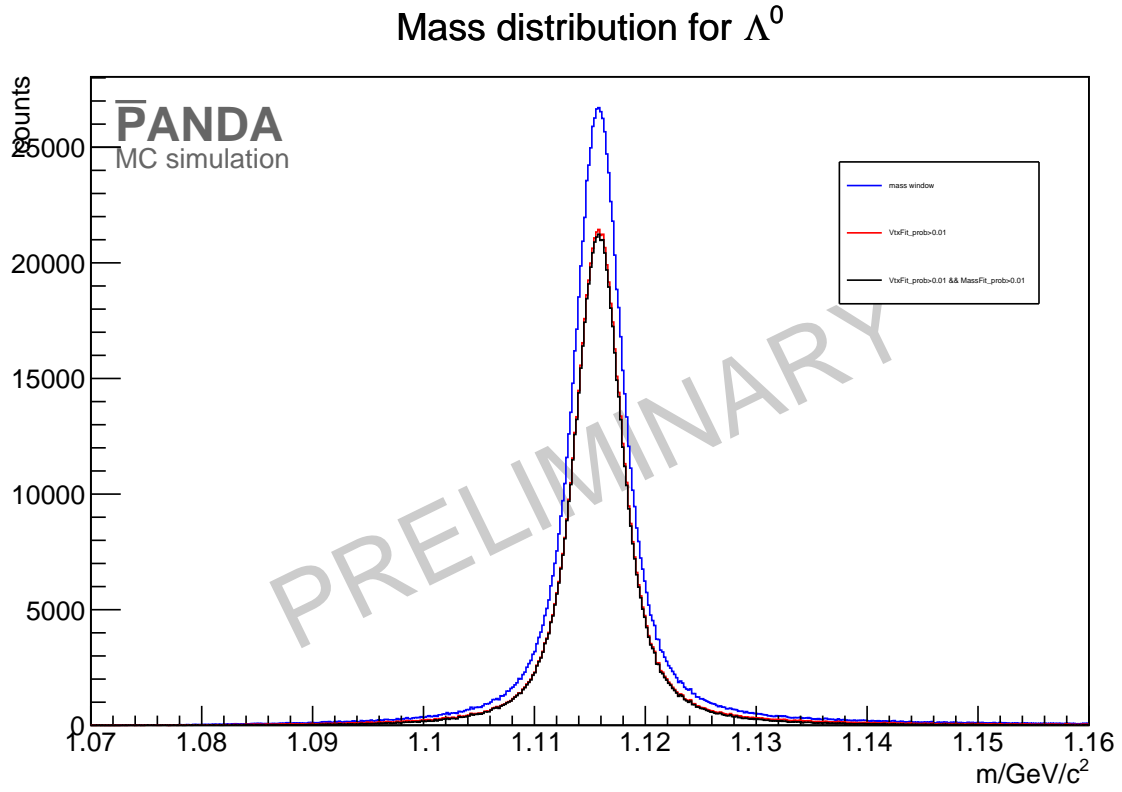


**Figure 2.4:** Mass distribution of  $\Lambda^0$  for different cuts

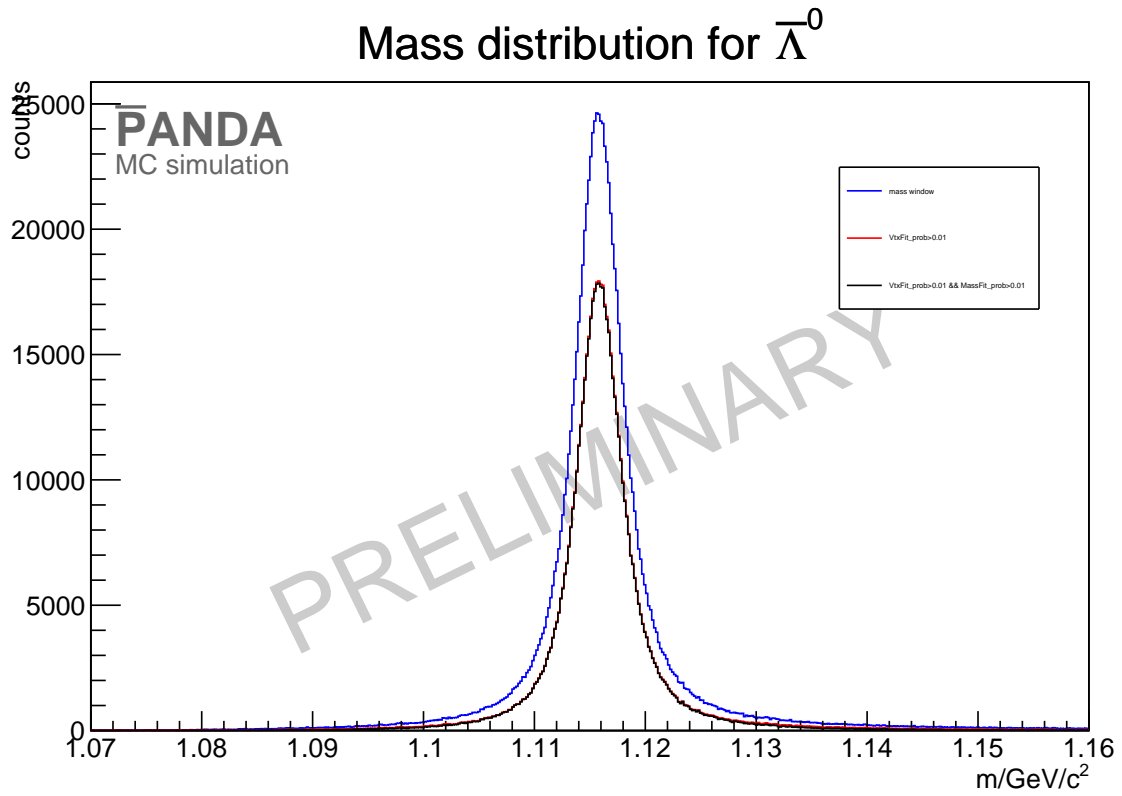


**Figure 2.5:** Mass distribution of  $\bar{\Lambda}^0$  for different cuts

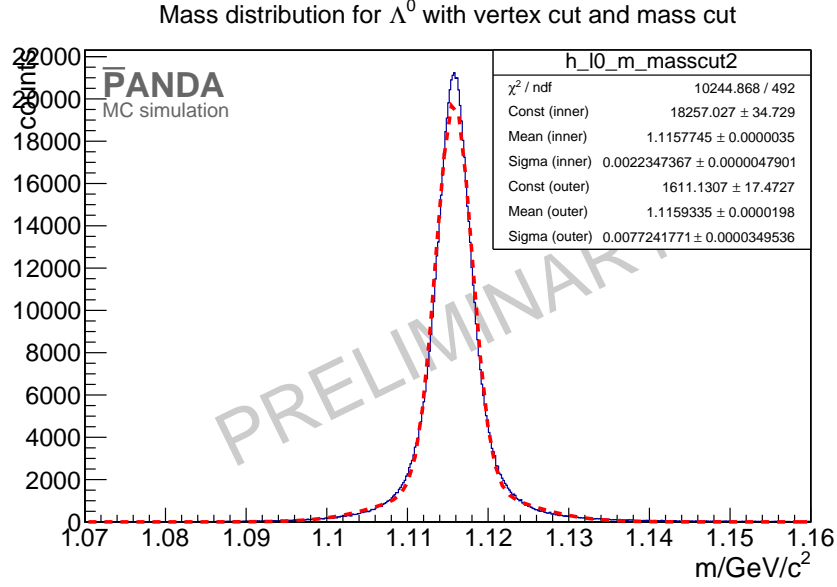


**Figure 2.6:** Mass distribution – blue line – for  $\Lambda^0$  fitted with a double Gaussian fit shown as red dashed line.

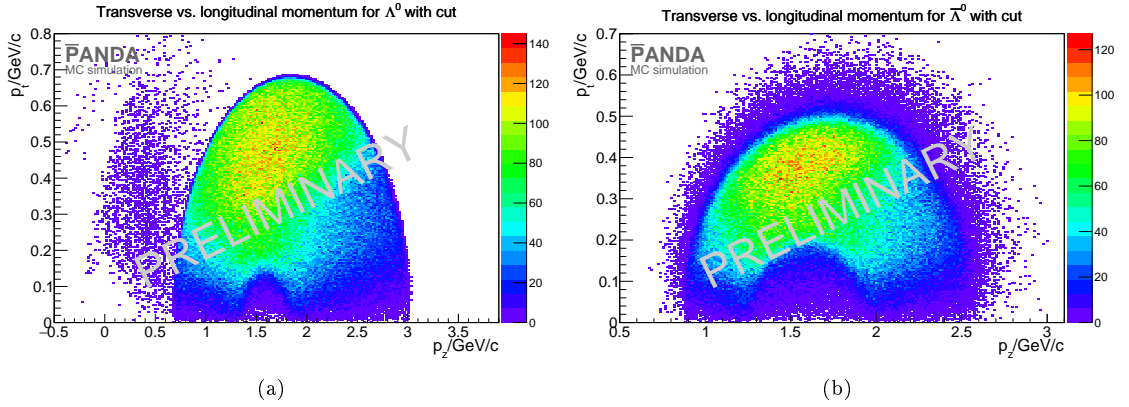


**Figure 2.7:** The plots shows the transverse against the longitudinal momentum for  $\Lambda^0$

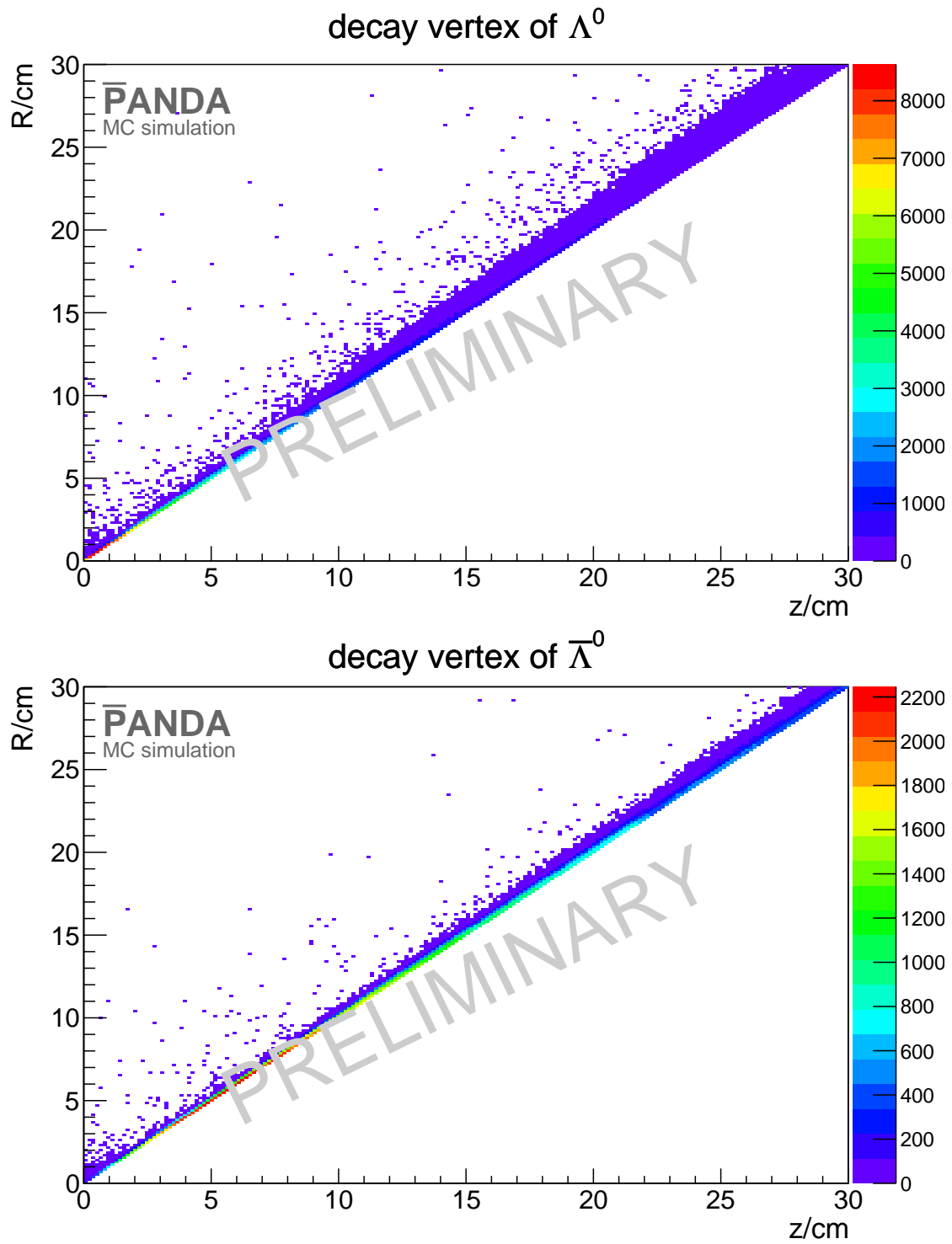


**Figure 2.8:** Upper plot shows the decay vertex of  $\Lambda^0$ ; lower plot shows decay vertex of  $\bar{\Lambda}^0$

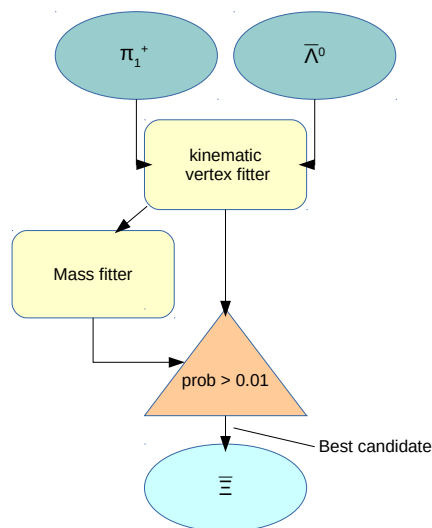


**Figure 2.9:** Scheme for  $\bar{\Xi}$  reconstruction

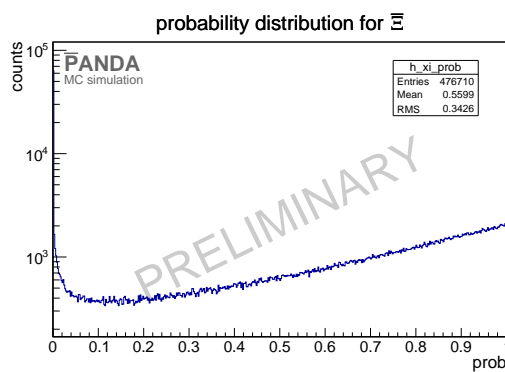


**Figure 2.10:**  $\chi^2$  probability for  $\bar{\Xi}$  reconstruction



**Table 2.3:** Vertex resolution for  $\Xi^-$  and  $\Xi^0$  (c.c. channel)

position	$\Xi^-$	$\Xi^0$ (from c.c.)
x/cm	0.052	0.056
y/cm	0.052	0.052
z/cm	0.192	0.2

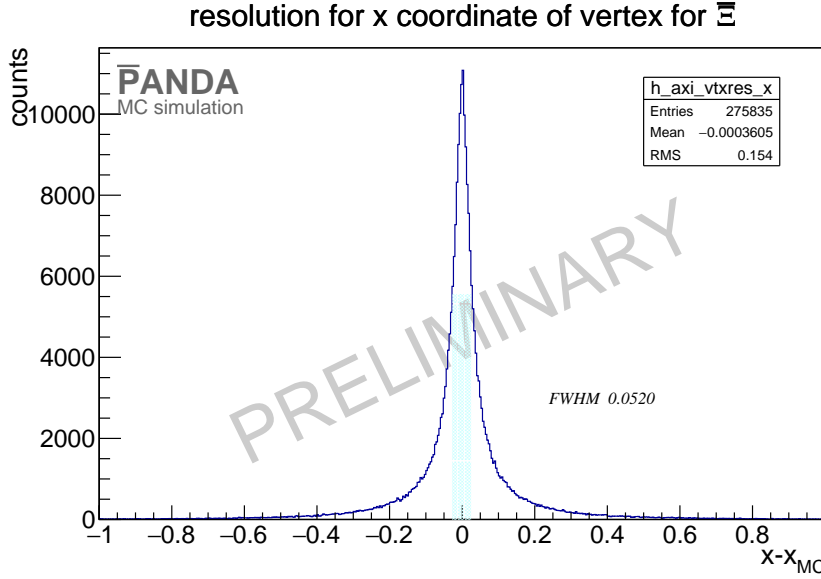


**Figure 2.11:** Vertex resolution of x position for  $\Xi^-$

## Results

The vertex resolution after all cuts is shown in table 2.3.

It is determined by calculating the full width at half maximum (FWHM) of the distribution. The advantage of using this method to calculate the vertex resolution is that the FWHM is independent of distribution shape. Figure 2.11 and Figure 2.12 show the vertex resolution. The mass distribution for the different cuts is shown in figure 2.13 and figure 2.14. The vertex fitter cut reduces the number of events most and the width of the mass distribution gets smaller.

After using all cuts on the mass distribution the reconstructed mass of  $\Xi^-$  and  $\Xi^0$  can be determined by a double Gaussian fit. This is exemplarily shown for the  $\Xi^-$  in figure 2.15.

The result of the mass fit is for  $\Xi^-$   $m = (1.3721716 \pm 9.2 \cdot 10^{-5}) \text{ GeV}/c^2$  and for  $\Xi^0$   $m = (1 \pm 1 \cdot 10^{-5}) \text{ GeV}/c^2$ . The two dimensional momentum distribution for  $\Xi^-$  and  $\Xi^0$  is shown in figure 2.16

The reconstruction efficiency for  $\Xi^-$  is 18.39% and for  $\Xi^0$  18.64%.

## 2.4. Reconstruction of $\Xi(1820)$ and $\bar{\Xi}(1820)$

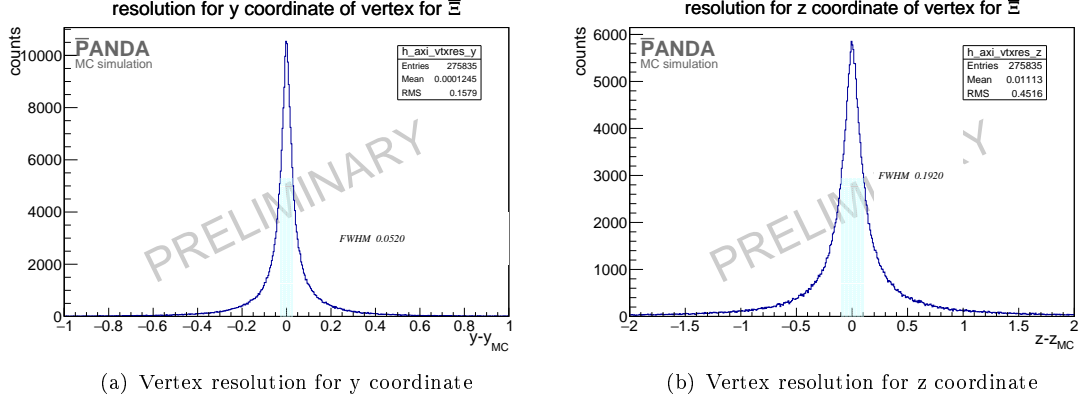


**Figure 2.12:** left plot: Vertex resolution of y position for  $\bar{\Xi}$ ; right plot: Vertex resolution of z position for  $\Xi$ .

**Table 2.4:** Vertex resolution for  $\Xi(1820)$  and  $\bar{\Xi}(1820)$ .

position	$\Xi(1820)$	$\bar{\Xi}(1820)$ (from c.c.)
x/cm	0.028	0.028
y/cm	0.028	0.028
z/cm	0.1	0.1

## 2.4 Reconstruction of $\Xi(1820)$ and $\bar{\Xi}(1820)$

### Selection

For the reconstruction of  $\Xi(1820)$  one combine  $\Lambda^0$  and  $K^-$  meson and for  $\bar{\Xi}(1820)$   $\bar{\Lambda}^0$  and  $K^+$  using the best candidate from  $\Lambda^0$  and  $\bar{\Lambda}^0$  and  $K^+$  and  $K^-$  with more than 3 hits in one of the inner tracking detectors. After the combination of the particles a mass window cut with width of  $0.3\text{GeV}/c^2$  is performed. The daughter particles are fitted then to a common vertex point with the PndKinVtxFitter. Only those candidates for  $\Xi(1820)$  ( $\bar{\Xi}(1820)$ ) are selected which have a fit probability of more then 1%. The selection scheme is shown in figure 2.17.

The  $\chi^2$  probability distribution for the vertex fit is shown in figure 2.18. The distribution is again not flat but increases for values up to one.

If there is more than one particle the best candidate is chosen.

### Results

The vertex resolution for  $\Xi(1820)$  and  $\bar{\Xi}(1820)$  is summarized in table 2.4.

Here again the vertex resolution is calculated with the FWHM. This is exemplarily shown for  $\Xi(1820)$  in figure 2.19 and figure 2.20.

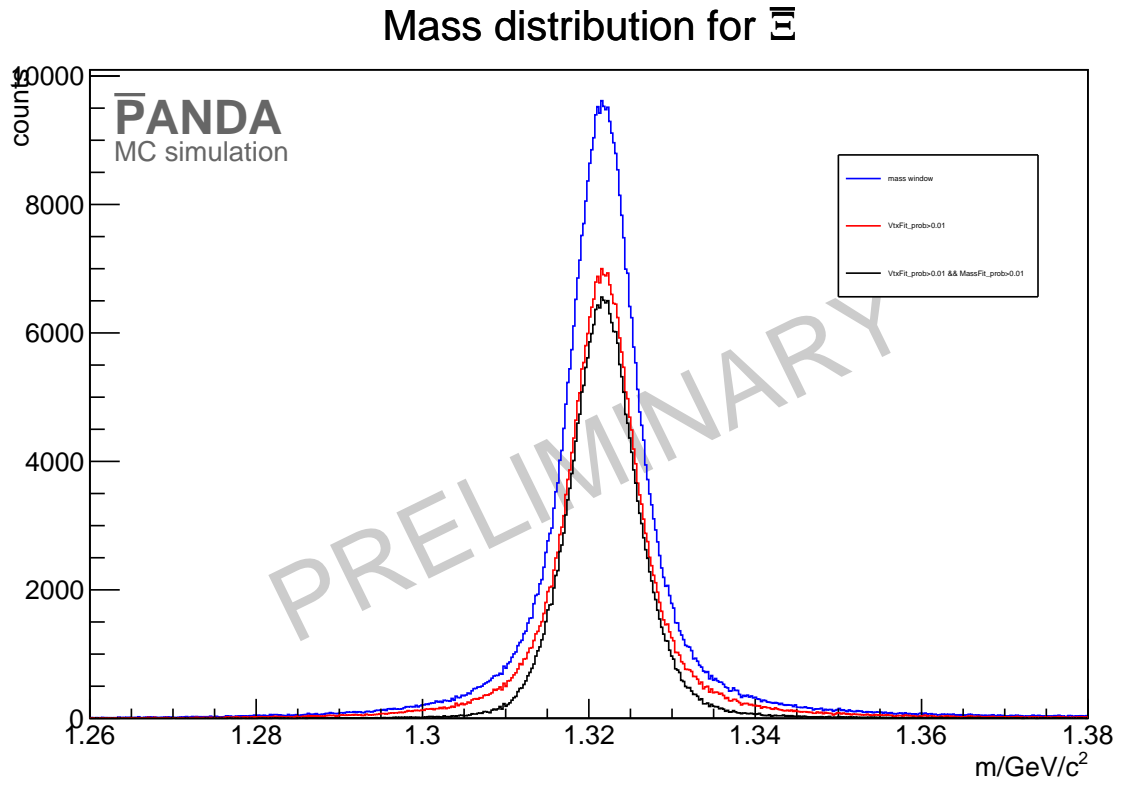


**Figure 2.13:** Mass distribution of  $\Xi^-$  for different cuts

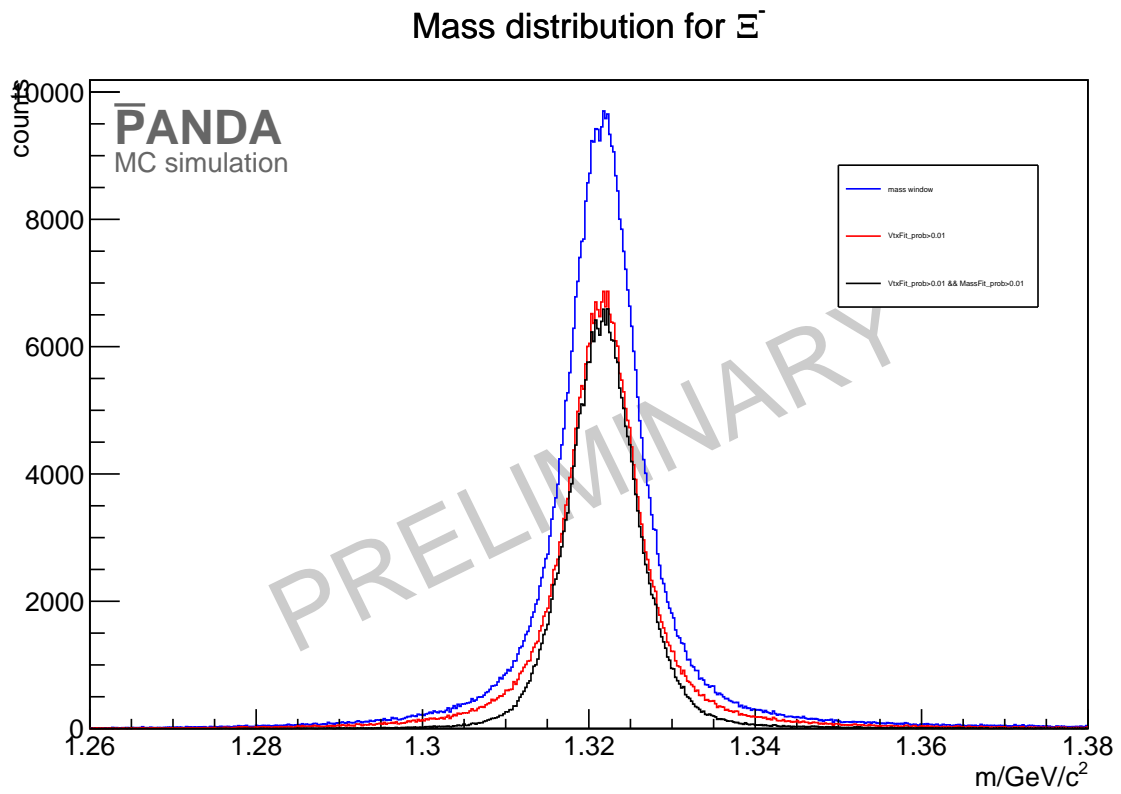


**Figure 2.14:** Mass distribution of  $\Xi^-$  for different cuts

## 2.4. Reconstruction of $\Xi(1820)$ and $\Xi(1820)$

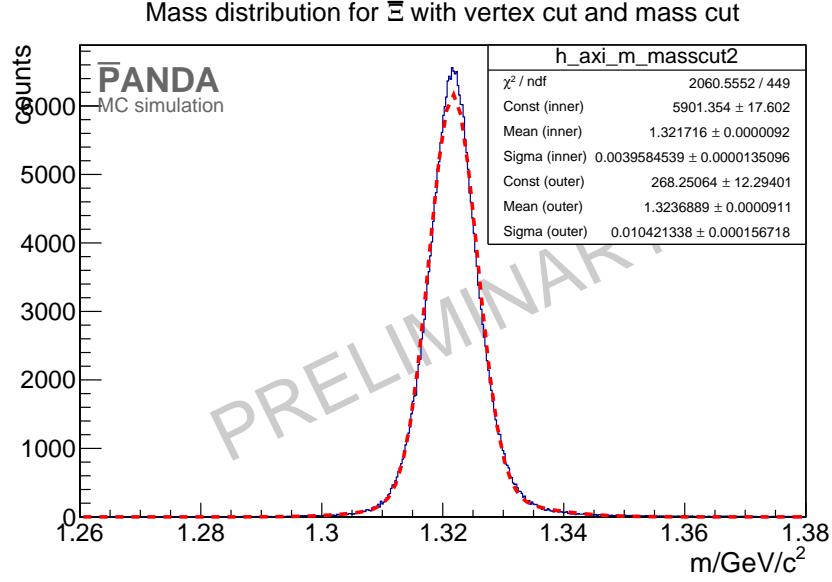


Figure 2.15: Mass fit with a double Gaussian fit

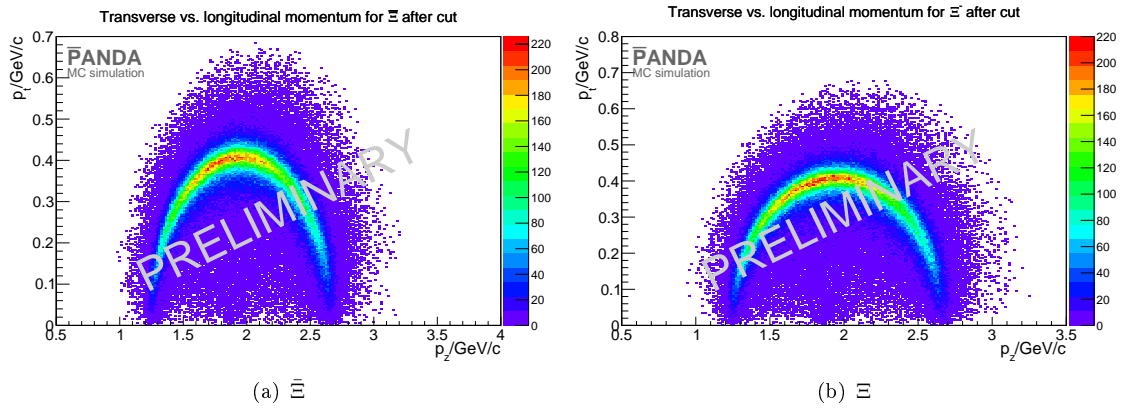
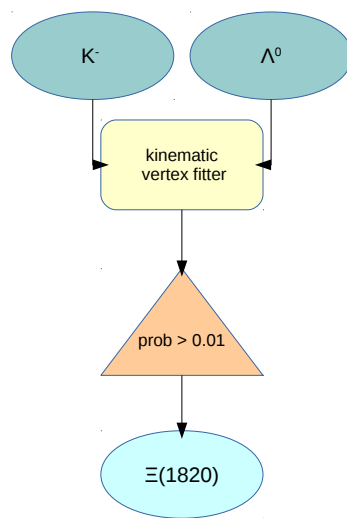


Figure 2.16: The plots shows the transverse against the longitudinal momentum for  $\Xi$  and  $\Xi$



**Figure 2.17:** Scheme for  $\Xi(1820)$  reconstruction

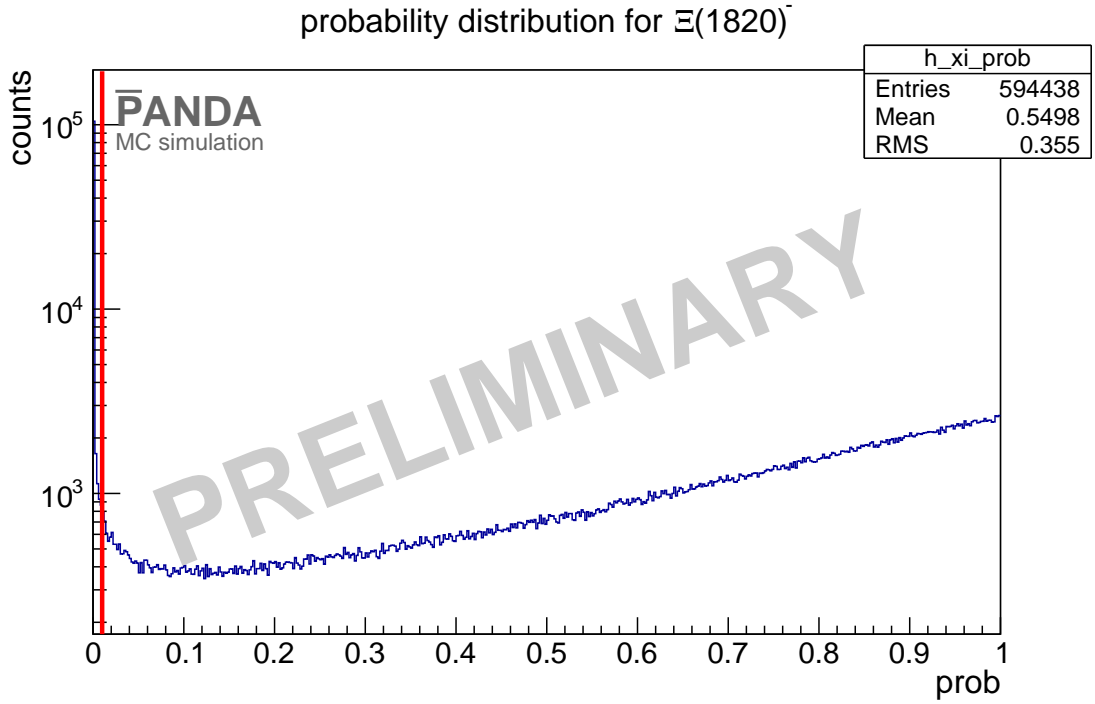


Figure 2.18:  $\chi^2$  probability distribution of kinematic vertex fit for  $\Xi(1820)$ .

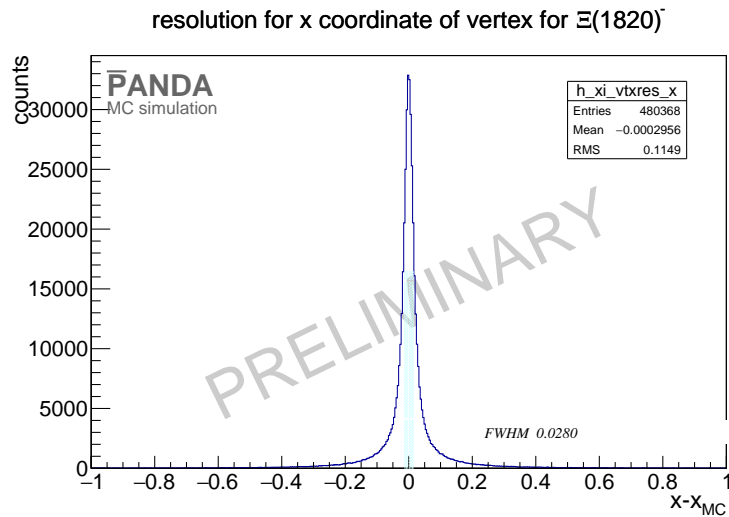
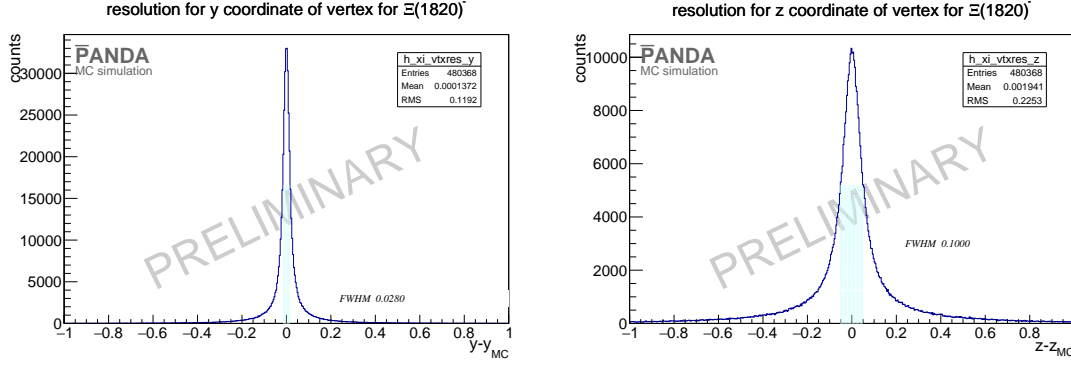


Figure 2.19: Vertex resolution of the x coordinate for  $\Xi(1820)$ .



(a) Vertex resolution of the y coordinate for  $\Xi(1820)$ . (b) Vertex resolution of the z coordinate for  $\Xi(1820)$ .

**Figure 2.20:** Figure a) shows the vertex resolution for the y coordinate and figure b) for the z coordinate of  $\Xi(1820)$

After performing the both fits and cut on the probability values, the mass for  $\Xi(1820)$  and  $\bar{\Xi}(1820)$  can be determined by fitting the mass with a double Gaussian fit. Figure 2.21 shows the mass distribution for both particles after each cut.

The mass fit is exemplarily shown for the  $\Xi(1820)$  in figure 2.22.

The mass values for the  $\Xi(1820)$  is fitted to  $1 \pm 1 \text{ GeV}/c^2$  and for  $\bar{\Xi}(1820)$  to  $1 \pm 1 \text{ GeV}/c^2$ . These values are close to the input value. Figure 2.23 shows the two dimensional momentum distribution. For both subplots the x axis shows the longitudinal momentum and on the y axis there is shown the transverse momentum.

The reconstructed distributions are in good agreement with the distribution coming from the simulated events which are shown in figure 1.3 (b).

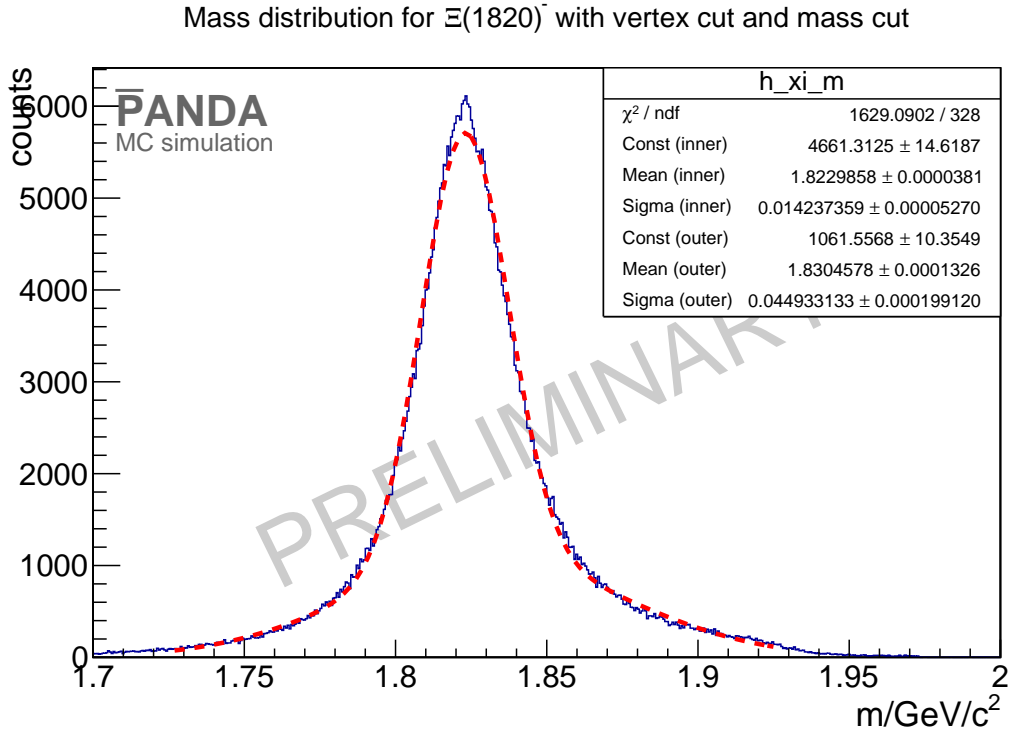
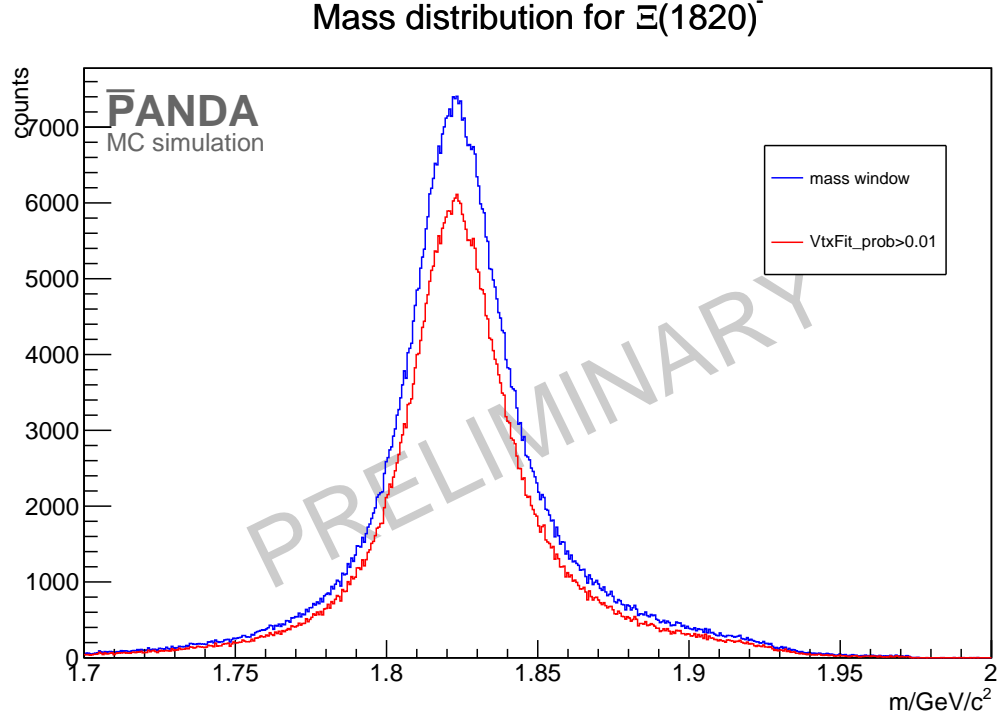
## 2.5 Reconstruction of hole chain

### Selection

To reconstruct the hole reaction chain  $\Xi(1820)$  and  $\bar{\Xi}$  are combined. This is also done with  $\bar{\Xi}(1820)$  and  $\Xi$  for the charge conjugated channel. For the event selection now it is use a excluding method. The four momentum vector of the daughter particles is fitted to the initial for momentum vector

$$(p_x, p_y, p_z, E) = (0, 0, 4.6, 5.63)$$

of the  $\bar{p}p$ . This fit is performed with the PndKinFitter. After the four momentum fit there were only those candidates selected which have a  $\chi^2$  probability of more than 1%. The  $\chi^2$





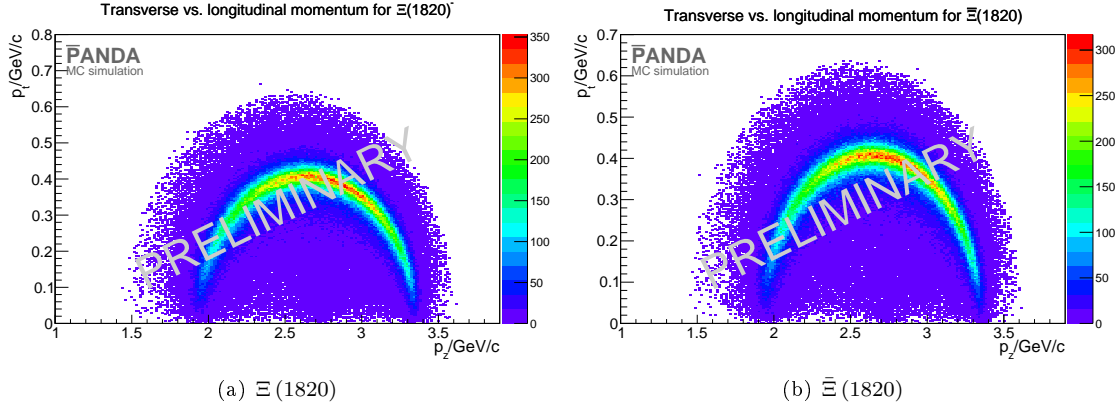


**Figure 2.23:** Both plots show the longitudinal versus the transverse momentum of the excited cascade baryon.

**Figure 2.24:** 4-constraint fit probability

probability is shown in figure 2.24. The red line denotes the cut value. The selection scheme is shown in figure 2.25

## Results

The results of the reconstruction efficiency for all non-final state particles is shown in table 2.5 and table 2.6.

How good the reconstruction works is shown in figure 2.26. This plot shows the Dalitz plot for the  $\bar{\Xi}$ ,  $\Lambda^0$  and  $K^-$  final states after the reconstruction. Compared with the Dalitz plot of the simulated particles which is shown in figure 1.4 the reconstruction seems to be good.

**Table 2.5:** reconstruction efficiency for non-final state particles for  $\bar{p}p \rightarrow \Xi(1820) \bar{\Xi}$

particle	reco efficiency in %	dp/p in %
$\Lambda^0$	50.3278	1.50497
$\bar{\Lambda}^0$	41.4625	1.45024
$\bar{\Xi}$	18.389	1.2889
$\Xi(1820)$	32.0245	2.67691
$\Xi(1820) \bar{\Xi}$ system	4.69293	1.03214

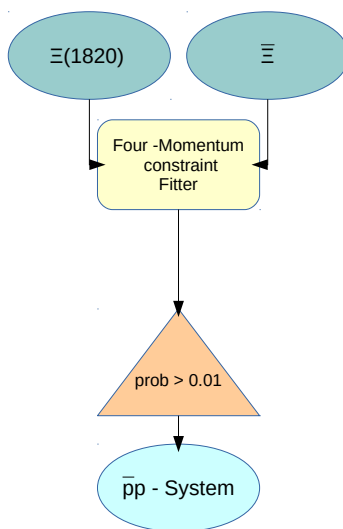


**Figure 2.25:** Scheme for 4-Constraint Fit

**Table 2.6:** reconstruction efficiency for non-final state particles for  $\bar{p}p \rightarrow \Xi(1820) \Xi$

particle	reco efficiency in %	dp/p in %
$\Lambda^0$	42.4693	1.45429
$\bar{\Lambda}^0$	48.9991	1.50196
$\Xi$	18.6405	2.29877
$\Xi(1820)$	33.2238	1.31081
$\Xi(1820) \Xi$ system	4.87227	1.03127

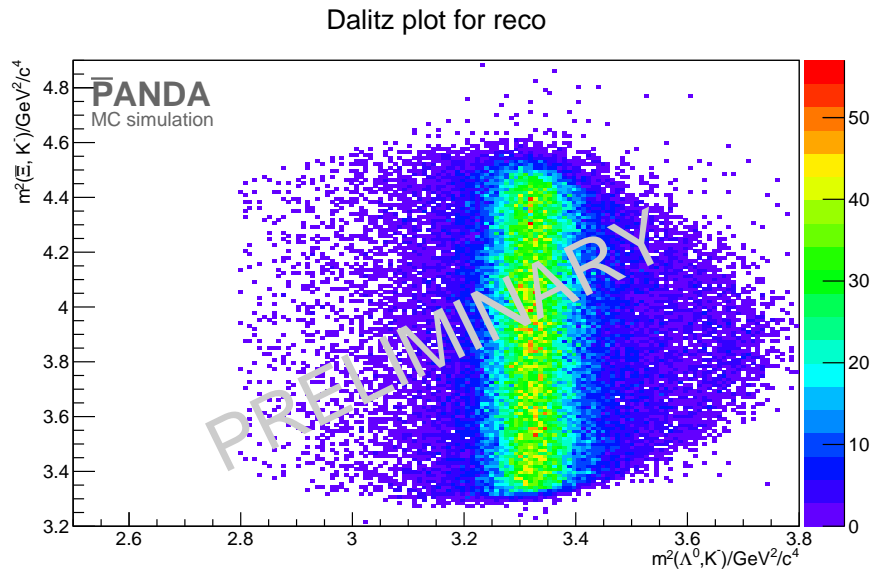


Figure 2.26: Dalitz plot for reconstructed particles

---

## 3 Background

---

## 4 Conclusion

Here should be the conclusion

---

## Bibliography

- [1] W. Erni, I. Keshelashvili, B. Krusche, M. Steinacher, Y. Heng, Z. Liu, H. Liu, X. Shen, O. Wang, H. Xu, *et al.*, “Physics performance report for panda: Strong interaction studies with antiprotons,” *arXiv preprint arXiv:0903.3905*, 2009.
- [2] J. B. et al., *Particle Data Group*. Phys. Rev. D86, 010001, 2012.